Comparing three-dimensional serial optical coherence tomography histology to MRI imaging in the entire mouse brain

Alexandre Castonguay
Joël Lefebvre
Philippe Pouliot
Frédéric Lesage

Comparing three-dimensional serial optical coherence tomography histology to MRI imaging in the entire mouse brain

Alexandre Castonguay,[a] Joël Lefebvre,[a] Philippe Pouliot,[a,b] and Frédéric Lesage[a,b,*]
[a]École Polytechnique de Montréal, Montréal, Québec, Canada
[b]Institut de Cardiologie de Montréal, Montréal, Québec, Canada

Abstract. An automated serial histology setup combining optical coherence tomography (OCT) imaging with vibratome sectioning was used to image eight wild type mouse brains. The datasets resulted in thousands of volumetric tiles resolved at a voxel size of $(4.9 \times 4.9 \times 6.5)$ μm^3 stitched back together to give a three-dimensional map of the brain from which a template OCT brain was obtained. To assess deformation caused by tissue sectioning, reconstruction algorithms, and fixation, OCT datasets were compared to both *in vivo* and *ex vivo* magnetic resonance imaging (MRI) imaging. The OCT brain template yielded a highly detailed map of the brain structure, with a high contrast in white matter fiber bundles and was highly resemblant to the *in vivo* MRI template. Brain labeling using the Allen brain framework showed little variation in regional brain volume among imaging modalities with no statistical differences. The high correspondence between the OCT template brain and its *in vivo* counterpart demonstrates the potential of whole brain histology to validate *in vivo* imaging. © 2018 Society of Photo-Optical Instrumentation Engineers (SPIE) [DOI: 10.1117/1.JBO.23.1.016008]

1 Introduction

Light microscopy remains the main tool used to investigate cellular structure. Over the past decades, advances in this field gave rise to new imaging techniques,[1–4] generating new contrast information at the cellular level. To this day, microscopic imaging of cellular tissue, commonly termed histology, remains the gold standard for histopathologists. While histology has had tremendous impact on our understanding of the brain anatomy and function, observation under a microscope of a thin slice of tissue gives a very poor representation of the whole organ. There is an increasing consensus among brain scientists toward the importance of neuronal pathways among brain regions to understand neurodegenerative diseases and brain injury.[5–9] Serial histology to obtain large tissue section datasets is becoming essential to help bridge spatial scales among imaging at the cellular level and morphology at the millimeter scale.

This need was demonstrated with the Big Brain initiative,[10] where 7400 histological slides of a single human brain were cut, digitized, and stitched back together to yield an entire brain resolved at 20 μm and totaling 1 Tb of data. However, this was a labor-intensive work, where each slice was manually placed on glass plates and corrected for cutting defects. Recent developments of automatic tools combined with microscopy allowed to overcome the need for manual operations, thus drastically reducing acquisition time. For example, micro-optical sectioning tomography[11] was introduced to automatically image entire mouse brains at a resolution of $(0.33 \times 0.33 \times 1)$ μm^3. While these techniques are important advances in bridging micrometric microscopy and whole brain imaging, they also include

limitations. Indeed, they are based on the imaging of cut tissue sections. In turn, sectioning leads to deformation and loss of tissue in the axis transverse to the movement of the cutting blade, making it difficult to recover the three-dimensional (3-D) topology. Moreover, depth subsampling, typically resulting in a resolution equal to the thickness of the cut, makes it difficult to properly represent the tissue in three dimensions. These difficulties can be overcome by combining vibratome sectioning to cut fresh tissue with depth-resolved imaging techniques, such as optical coherence tomography (OCT)[12,13] or two-photon microscopy.[14,15]

With the acquisition of whole brains at the micron scale, there is a growing interest to correlate these datasets rich in information to *in vivo* magnetic resonance imaging (MRI) imaging. For this, further validation is required to confirm that vibratome sectioning of tissue does not significantly alter the tissue's morphology. Moreover, tissue fixation is known to induce deformations in biological tissues, with the deformation varying widely depending on the fixation procedure used and fixation duration.[16,17] For instance, the absence of transcardial perfusion in mice will result in a slow diffusion of fixative in the brain, which could result in anisotropic deformation. Also, dehydration of tissue preceding microtome sectioning can also lead to considerable deformation. An evaluation of deformation produced by these serial histology techniques is necessary to correlate whole brain histology with *in vivo* MRI.

With the goal of evaluating such deformations, we developed a large scale motorized OCT scanner that is able to sequentially slice through agarose-embedded tissue. The developed imaging platform, which we named the slicer in this work, allows imaging of large sections of exposed intact tissue, before removing

*Address all correspondence to: Frédéric Lesage, E-mail: frederic.lesage@polymtl.ca

a thin slice with a vibratome to expose new tissue. Postprocessing algorithms are then used to reconstruct a 3-D dataset of entire small animal organs.

To measure deformation caused by fixation, serial sectioning, and to validate reconstruction algorithms, we imaged mouse brains with three distinct acquisitions. First, *in vivo* MRI datasets were acquired in anesthetized mice, followed by *ex vivo* MRI imaging of the same brains. The brains were then embedded in agarose blocks and imaged with the OCT serial scanner. With OCT, brain tissue displayed high contrast in white matter due to changes of the refractive index in white matter fiber tracts.[13,18,19] Despite the fact that signal intensity originating from white matter was highly dependent on fiber tract orientation, coregistration to MRI was feasible and robust. In this work, we adapted an automatic and standardized pipeline workflow, based mainly on the Advanced Normalization Tools (ANTs),[20] to perform groupwise and individual comparison among imaging modalities. Anatomical MRI imaging methods that have been used to study brain morphology, such as cortical thickness and anatomical labeling were applied to OCT imaging to compare modalities for deformations.

More specifically, in this work, we imaged a group of brains using serial histology and used MRI image processing tools to perform statistical group analysis on these large histological datasets of entire mouse brains. Our results show that there is no significant deformation produced by the different stages of brain tissue manipulation (fixation and slicing). To our knowledge, this is the first attempt at registration of whole organ histology to MRI volumes, opening the way for studies accessing microscopic validation of *in vivo* MRI observations. We also compute for the first time an average brain atlas based on OCT reflectivity that can be used to find new insight to white matter contrast in OCT.

2 Materials and Methods

2.1 In Vivo Measurements

A total of $N = 8$ male 3-month-old C57Bl/6 wild type mice were used for this study. The Animal Research Ethics Committee of the Montreal Heart Institute approved all surgical procedures, which were performed according to the recommendations of the Canadian Council on Animal Care. Mice were anesthetized with isoflurane (2%) and imaged in a 7-T MRI (Agilent 7T-30), equipped with a 12-cm-inner diameter gradient coil insert (gradient strength 600 mT/m, rise-time 130 μs), with a true fast imaging with steady-state precession sequence (TFISP),[21] using a volume coil for transmission and head surface coil for reception (Rapid Biomedical, Germany). TR/TE = 6.0/3.0 ms, $256 \times 256 \times 192$ matrix, with a longitudinal readout direction, $18 \times 18 \times 13.5$ mm field of view (FOV) for a nominal 70-μm isotropic resolution, with a fractional anisotropy (FA) = 35 deg, 4 frequency shifts, and 6 averages for a 120-min scan duration. To account for potential deformation due to gradient calibration, voxel size was further calibrated using a phantom of known size and measured at 77 μm.

2.2 Ex Vivo Measurements

One week following *in vivo* imaging, mice were euthanized to extract the brain. They were first anesthetized under 2% isoflurane and transcardially perfused with 20 ml of saline, followed by a mixture of 4% paraformaldehyde mixed with 1% gadolinium

at a rate of 2 ml/min. For *ex vivo* MRI imaging, four brains were extracted from the skull while the four others were left in the cranium and placed in a degassed Fomblin solution to reduce undesired MRI signal from the exterior of the brain.[22,23] The TFISP sequence was used at increased resolution, TR/TE = 18/9 ms, $600 \times 480 \times 480$ matrix, $15 \times 12 \times 12$ mm FOV, for a nominal 25-μm isotropic resolution, adjusted to 27 μm with the calibration above, with FA = 10 deg, 16 frequency shifts, no average, and an 18-h 20-min scan duration.

2.3 Serial Optical Coherence Tomography Measurements

2.3.1 System operation

Two weeks after euthanization, the mouse brains were embedded in 4% agarose for *ex vivo* slicer imaging. Tissue samples were embedded in a cylindrical agarose block and placed underneath the microscope objective. To overcome limited light penetration in the tissue from microscopic imaging, a vibratome was used for sequential sectioning of tissue to reveal new tissue to image. To expose coronal sections of the tissue, all brains were placed with the antero-posterior axis vertically with the cerebellum facing the microscope's objective. Following the design described in Ref. 15, a dual-flexure isolated vibration of the blade with a DC motor on a one axis transverse movement provided precise cutting of fresh (unfrozen) tissue [Fig. 1(a)]. X and Y stages moved the sample relative to the objective allowing to image every subregion (2.5×2.5 mm) of the tissue plane. After each section was imaged, a Z stage raised the sample by 200 μm to remove a slice of equivalent thickness, and the process was repeated automatically. The Z position of the sample was adjusted to have the focus ∼50 μm under the tissue surface, thus avoiding imaging of tissue deformed by slicing. For more details regarding automated serial histology, see Ref. 15.

2.3.2 Optical setup

Data acquisition was performed using a custom-made fibered optical coherence tomography scanner. The OCT system uses a swept-source laser (Axsun, 1310 Swept Source Engine) with an output power of 18 mW. The central wavelength of the laser is $\lambda = 1310$ nm with tuning bandwidth of $\Delta\lambda = 100$ nm. A 50-kHz sweeping rate enabled high-speed imaging. Light exiting the fiber in the sample arm was deflected by X and Y galvanometers before passing through a telescope ($f_1 = 35$ mm and $f_2 = 100$ mm) to enlarge the beam diameter at the entrance of the pupil of a 3× telecentric air objective (Thorlabs, LSM04), giving a lateral resolution of 8 μm in water. A custom-made coverslip was added between the objective lens and the sample to avoid water ripples and maintain a constant water column length in the sample arm of the OCT. The addition of a variable thickness of glass in the reference arm was necessary to compensate dispersion caused by lens and water in the sample arm. Axial resolution was measured at 10 μm in water. Individual OCT volumetric datasets were composed of 1152 points per A-line, 512 A-lines per B-scan, and 512 B-scans per C-scan, resulting in an OCT volume in a little over 5 s. During acquisition, volumetric data were discarded for depths over 780 μm due to out-of-focus effects and high signal attenuation. The use of a low-magnification microscope objective and rapid imaging with a swept-source OCT enabled imaging entire mouse brains within ∼8 h.

2.4 Data Processing

2.4.1 Optical coherence tomography data reconstruction

The first reconstruction step was to transform the volumes to isotropic voxels and to correct for optical artifacts introduced by the objective. A displacement model of the motorized stage was then used to estimate each tile position within the mosaic. This model considered the angle between the X and Y motors, the angle between the motor axes and the laser scanning plane, and the overlap size among neighboring tiles. The model parameters were estimated from the data by computing the phase-correlation-based pairwise registration of all neighboring tiles within the mosaic and by inverting the model, solving for each parameter. Using this method, the individual tile XY position within each slice was obtained.

The next step was to stitch together the volumes for each slice [Fig. 1(b)]. This was done using linear blending to fuse overlapping tiles

$$M'(x, y) = \alpha(x, y)I(x, y) + [1 - \alpha(x, y)]M(x, y), \qquad (1)$$

where $M(x, y)$ is the mosaic, $I(x, y)$ is a tile, and $\alpha(x, y)$ is the spatially varying blending weights, obtained by solving the Laplace equation $\nabla^2 \alpha(x, y) = 0$ with Dirichlet boundary
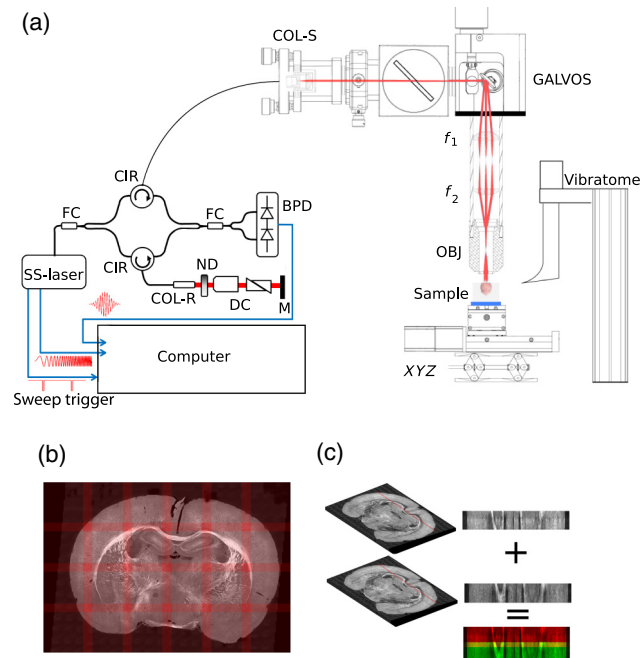

(a)

(b)   **(c)**

Fig. 1 Serial scanner overview: (a) microscopic imaging platform. The fibered swept-source OCT enters the microscope at COL-S. Galvanometric mirrors (GALVOS) allow light passing through a telescope ($f_1 = 35$ mm and $f_2 = 100$ mm) and 3× objective (OBJ) to scan the surface of the sample. X, Y, and Z stages (XYZ) allow movement of the sample relative to the objective and cutting 200-μm slices with a vibratome. Right side of (a) shows the OCT setup. SS-laser, swept-source laser; FC, fiber coupler; CIR, circulator; COL-R, collimator for reference arm; ND, neutral density filter; DC, dispersion compensation glass; M, mirror; BPD, balanced photodetector; and COL-S, collimator for sample arm. (b) Slice assembly. Each tile is stitched by assembling individual tiles. A 20% overlap among neighboring tiles (red label) was fused using a Laplace blending. (c) Tissue slices stitching. Each reconstructed slice has a thickness of 260 μm. Considering cuts at every 200 μm, there is an 60-μm overlap among slices.

conditions over their overlap region. This was proven adequate for complex overlap geometries and ensuring a smooth transition among neighboring tiles. The last reconstruction step was to stitch the slices together in the Z-direction to get a complete 3-D volume [Fig. 1(c)]. This was done by computing the shift among adjacent slices using the cross correlation of their two-dimensional image gradient magnitude and using the same blending method as for the XY stitching. This reconstruction resulted in a 3-D map of the brain tissue optical reflectivity at a microscopic resolution.

The OCT reflectivity data were affected by a depth-dependent signal attenuation due to the microscope's confocal point spread function (PSF) and to tissue scattering and absorption. To compensate this effect, the PSF was first extracted from the surrounding agarose using a Gaussian beam model

$$\mathrm{PSF}(z) = \left[\left(\frac{z - z_f}{z_R} \right)^2 + 1 \right]^{-1}, \qquad (2)$$

where z is the depth, z_f is the focal plane depth, and z_R is the effective Rayleigh length. An XY invariant synthetic axial PSF was generated from the fitted model and used to remove the signal roll-off. Then, a single scattering photon model was used to estimate the tissue attenuation coefficient locally.[24,25] The attenuation at a given depth i is defined as

$$\hat{u}(i) = \frac{1}{2\Delta z} \log \left[1 + \frac{I(i)}{\sum_{j=i+1}^{\infty} I(j)} \right], \qquad (3)$$

where Δ is the axial resolution and I is the signal intensity. Finally, using the Beer–Lambert law, an attenuation bias field was computed for each slice as

$$B(x, y, z) = \exp \left[-2 \int_0^z u(x, y, z) \mathrm{d}z \right] \qquad (4)$$

and used to normalize the data

$$I'(x, y, z) = \frac{I(x, y, z)}{B(x, y, z)}. \qquad (5)$$

The necessary time for the whole data reconstruction process remained under 12 h/brain. More details regarding the OCT data reconstruction and attenuation compensation can be found in Ref. 26.

2.4.2 Brain masking

For MRI images, a bias field correction (*N4BiasFieldCorretion*) implemented in the ANTs toolkit was applied[27] before brain masking. The primary step for subsequent analysis of data was to create an efficient brain mask, isolating the brain from surrounding tissue (i.e., skull) and background noise. For all three imaging modalities, an automatic brain extraction algorithm was written using the open-source scikit-image toolbox[28] for reliable and repeatable masking. The brain volumes were thresholded using the Otsu method[29] and underwent a morphological erosion (radius = 2). The resulting binary mask was multiplied with the original volume to initiate extraction using morphological snakes, an iterative contour evolution method to detect edges.[30,31] For both *in vivo* and *ex vivo* MRI, the obtained brain mask was then applied to the original brain volume, and a new

field bias correction was applied to the masked MRI original data to avoid contributions from nonbrain tissue.

2.4.3 *Atlas registration*

Brain registration was performed using the ANTs toolkit[20,32,33] and the anatomical Allen mouse brain atlas generated from native two-photon autofluorescence features of 1675 specimens.[14,34] First, brains were aligned with a rigid transformation to the Allen atlas, which consists of a translation and a rotation of the dataset to best-fit the atlas orientation. Registration of MRI and OCT brain volumes to a mouse brain atlas allowed automatic segmentation of the brains by anatomical regions instead of biased and time-consuming manual segmentation. To bring the Allen atlas in the imaged brain stereotaxic space, a series of rigid, affine, and symmetric normalized (SyN) transformation, developed in the ANTs toolkit, were sequentially applied to fit the Allen template to the individual subject stereotaxic space. Figure 2 summarizes the data processing workflow used for subject registration. Mutual information was used as a cost function since datasets are imaged using different modalities, thus exhibiting different contrast information. Registration was a greedy computational process, and a downsampling of the OCT brains to 25-μm isotropic voxels was necessary to run coregistration. They found diffeomorphic transformation was then applied to the annotation file to bring it in the measurement space, resulting in an annotation map of the specimen. To determine registration quality, each *ex vivo* MRI brain was registered to their corresponding OCT image dataset as well as their corresponding labels. By measuring the overlap of brain subregions, we were able to quantify registration quality using the Jaccard metric, defined as the size of the overlap of two volumes divided by the size of the union of the same volumes.

A population template brain for each of the three imaging modalities was computed as described in the ANTs toolkit.[35] For each imaging modalities, the brain template was flipped along the midsagittal plane, and both original and mirrored brains were averaged using the same process, having the practical effect of doubling the number of brains for the template.
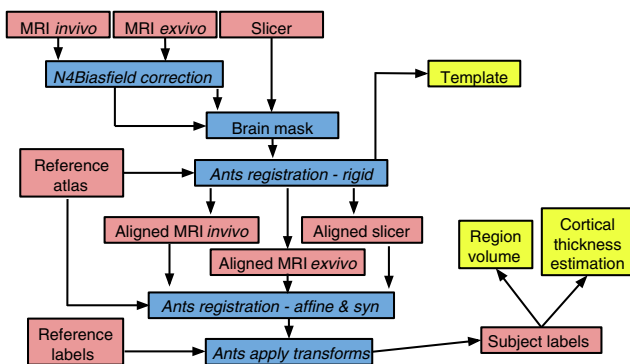

Fig. 2 Data processing workflow. Each MRI volume undergoes a nonuniformity bias field correction. Volumes are then masked to extract brains and undergo a rigid transformation (translation and rotation) to be aligned in the Allen framework. The aligned brains are then used to create three templates for each imaging modality. The Allen atlas is registered to each individual aligned brain using a combination of affine and SyN transformations. Allen atlas labels are transformed to subject space and used to determine large brain region volumes and cortical thickness. Red boxes: datasets, blue boxes: computational processes, italic: ANTs toolbox, and yellow boxes: outputs.

2.4.4 *Cortical thickness*

Cortical thickness has been used as a metric to evaluate morphological changes in various pathologies, such as Alzheimer's disease and schizophrenia,[36,37] its measure remains, therefore, of utmost importance. Here, we used a Laplacian thickness approach to measure cortical thickness. This algorithm uses the Laplace equation to compute equidistant lines through the cortex and to use orthogonal projections to compute cortical thickness.[38] Since the algorithm was optimized for human brains, input parameters were adapted to the brain size of mice (prior thickness = 1 mm, dT = 0.001).

3 Results

The template formation allowed for *in vivo* MRI to enhance the contrast between white and gray matter [Fig. 3(a)] compared to individual acquisitions (not shown). The TFISP sequence used for *ex vivo* MRI generated banding artifacts, which were significantly reduced upon template formation [Fig. 3(b)]. For serial-OCT imaging, the resulting template significantly smoothes transitions among slices and fades out cutting errors to show a highly detailed map of gray and white matter [Fig. 3(c)]. However, certain artifacts remain apparent in the OCT brain template. As expected, high contrast appears in myelinated fiber tracts, which is not constant within the same white matter structure. Green arrows in Fig. 3(c) highlight fiber tracts where reflectivity signal varies spatially for the corpus callosum [Fig. 3(c), left panel] and for the anterior commissure [Fig. 3(c), right panel]. Fibers running in the coronal plane appear as bright as others, perpendicular to the coronal sections appear darker, consistent with previous observations.[12,39] The OCT reflectivity brain template was made publicly available online.[40]

The resemblance of each individual sliced brain and the OCT brain template was assessed by looking at the warp fields used to pass from an original brain to the template. Warp fields resulting from the registration process provide the displacement of each voxel in three dimensions. By taking the modulus in 3-D for each voxel, we obtained a map of voxel displacements. Figure 3(d) shows a histogram of the average voxel displacement from each individual to the template for in all three imaging modalities. All three imaging modalities show a log-normal distribution. Both *in vivo* and *ex vivo* MRI imaging show very similar profiles, with average voxel displacements of 82 and 86 μm, respectively. The larger profile of the voxel displacement for slicer imaging suggests a wider range of voxel displacement and averages at 128 μm.

To check the similarity between the *in vivo* MRI and slicer templates, we used ANTs to warp one template on the other. Figure 4(a) shows the color-coded voxel displacement map between the slicer template and the *in vivo* MRI template, overlapped on a transversal section of the *in vivo* template. Largest voxel displacements appear in the olfactory bulb, the cerebellum, and in the optic nerve (not shown). These areas of large displacement translate into an extended tail in the voxel displacement histogram [Fig. 4(b)], toward higher displacements. These regions are either absent or partially absent of the OCT template due to slicing difficulties in these regions. Large displacements also occur in and around ventricular areas [Fig. 4(a)] whereas low displacement occurs in gray matter areas. The average voxel displacement in the whole brain is 74 μm.

To further investigate the deformation among imaging modalities, we measured large brain regions volumes. Large
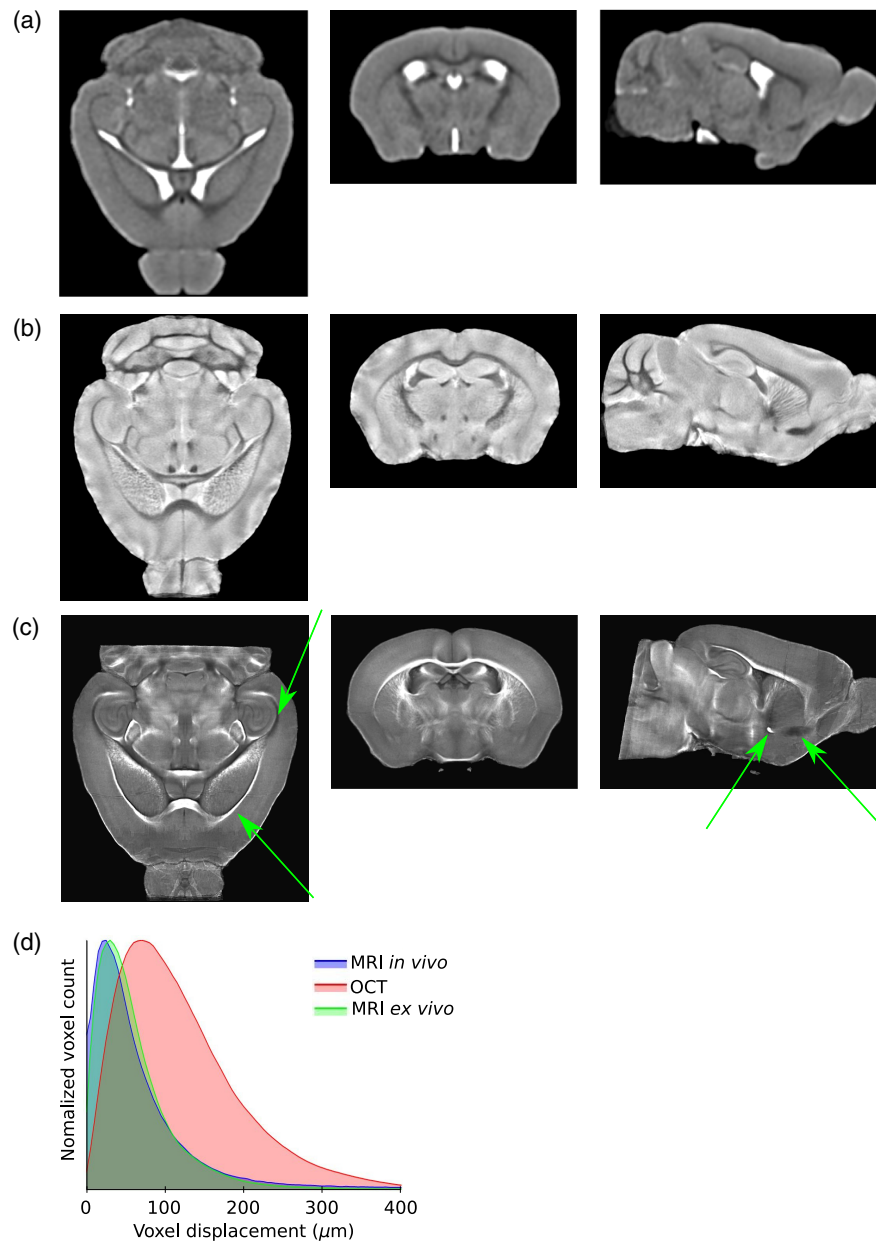
Fig. 3 Brain templates obtained with (a) *in vivo* MRI, (b) *ex vivo* MRI, and (c) slicer imaging viewed in orthogonal planes. Green arrows in (c) show white matter fiber tracts presenting different contrast within the anterior commissure (right panel) and the corpus callosum (left panel). (d) Normalized voxel displacement histogram. Voxel displacement within each brain map to the template, for three imaging modalities (blue: *in vivo* MRI, green: *ex vivo* MRI, and red: slicer).

brain regions annotation maps were aligned to subject brains [Fig. 5(a)] as described previously. Voxel counting within each region allowed estimation of volume [Fig. 5(b)]. Ventricles showed the largest volume variation between *in vivo* and *ex vivo* imaging. A shrinking to $47\% \pm 15\%$ of its *in vivo* volume was observed in both *ex vivo* imaging modalities. Other deep brain regions showed little variation in size (Table 1).

Volumetric variations for all deep brain structures were comprised within error bars, defined as the standard deviation over the mean. Cortical volume remained constant among imaging modalities, as for total brain volume. Paired *t-tests* among different imaging modalities showed no significant volumetric difference among large brain regions, except for the ventricles, where

a significant ($p < 0.05$) volume variation was observed between *in vivo* and *ex vivo* MRI and between *in vivo* and slicer imaging.

We used the Jaccard coefficient to check whether the registrations between two datasets were adequate for brain labeling. To do so, we first aligned each *ex vivo* MRI brain to its slicer counterpart. We then applied the same transformation to the large brain region labels of *ex vivo* MRI to align them with the labels of slicer imaging. The Jaccard coefficient, which gives an index of the similarity among aligned brains, is defined as the ratio of the intersection divided by the union of two volumes

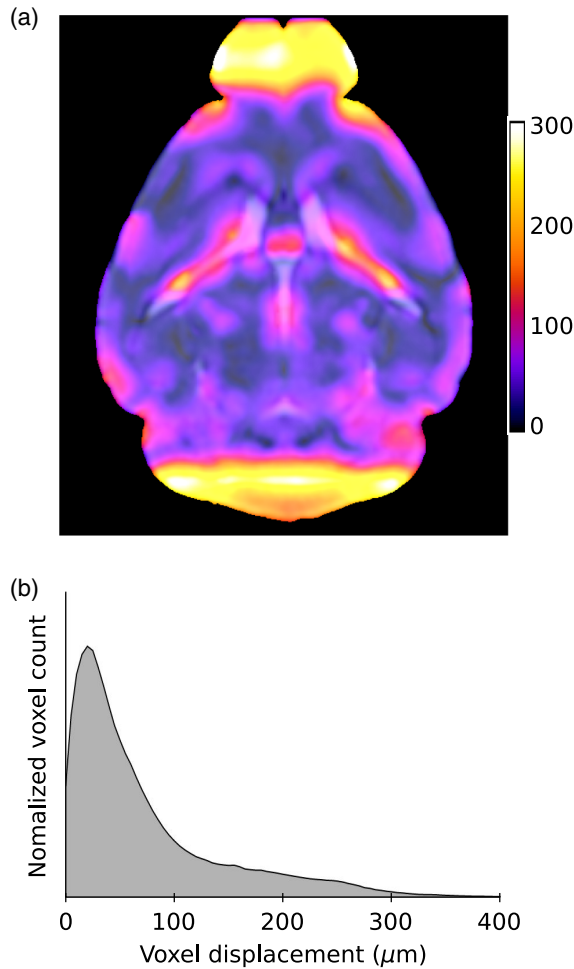$$J(A, B) = \frac{|A \cap B|}{|A \cup B|}, \tag{6}$$

(a)

(b)

Fig. 4 Warp field for slicer template to *in vivo* MRI template. (a) Transversal view of average voxel displacement overlapped on its corresponding transversal view of *in vivo* MRI template. Scale bar in μm. (b) Histogram of voxel displacement from slicer template to *in vivo* MRI template.

Table 1 Brain structure volumes measured with three different imaging modalities. Error represents standard deviation.

Brain structure	*In vivo* MRI (mm^3)	*Ex vivo* MRI mm^3)	Slicer (mm^3)
Ventricles	5.6 ± 0.38	$2.5 \pm 0.4^*$	$2.8 \pm 0.8^*$
Corpus callosum	7.9 ± 0.3	8.2 ± 0.5	8.4 ± 0.8
Thalamus	14.5 ± 0.4	13.7 ± 0.7	14.1 ± 1.3
Midbrain	20.5 ± 0.7	19.9 ± 0.8	20.2 ± 2.1
Caudoputamen	21.2 ± 0.7	22.0 ± 1.1	22.9 ± 2.0
Hippocampus	22.3 ± 1.2	23.6 ± 1.6	24.1 ± 2.4
Cortex	113 ± 3	113 ± 4	114 ± 7
Whole brain	442 ± 13	452 ± 16	414 ± 35

*Indicates statistical difference with *in vivo* at $p < 0.05$.

precise alignment of segmented cortex on template brain. Average cortical thickness was measured at 982 μm for *in vivo* imaging, 988 μm for *ex vivo* MRI imaging, and 1026 μm for slicer imaging. We were able to obtain a differential thickness map by subtracting the average thickness maps of the slicer to that of *in vivo* [Fig. 6(b), left panel] and *ex vivo* MRI [Fig. 6(b), right panel]. To evaluate whether these differential maps among imaging modalities were significant, we averaged the cortical thickness over large cortical areas (e.g., primary motor, primary somatosensory, and primary visual). A paired *t-test* with matching individuals showed no significant cortical thickness differences in large cortical areas between imaging MRI (*in vivo/ex vivo*) and slicer imaged brains.

4 Discussion

Serial sectioning and imaging proved to be an efficient means to image brain tissue at high resolution, giving a reliable representation of the *in vivo* tissue. By comparing large brain regions and whole brain volumes between *in vivo* and MRI *ex vivo* datasets, our results show that deformation caused by the fixation procedure used here is not significant compared to intramodal variations within a time period of two weeks postfixation. Previous work[16,17,41] has shown significant deformation caused by tissue fixation. However, our brain samples were transcardially perfused, allowing PFA to be uniformly distributed in the brain, instead of immersion of fresh brains in PFA,[16,17,41] which would result in slow and nonuniform diffusive perfusion. Also, for *ex vivo* imaging, brains did not undergo further fixative processes, such as ethanol dehydration, which further limited tissue deformation. Trial and error has also shown that diluting a 10% PFA solution to 4% in saline has had lower impact on tissue shrinking compared to powder based PFA.

The creation of an OCT template of the mouse brain was done for the first time and shown to be feasible with standard tools used in MRI. The ANTs toolbox proved to be an adequate tool and was able to converge to an optimal template without significant tuning. However, certain artifacts remain in the template brain as depicted previously. First, in the cerebellum, artifacts appear due to the folds that characterize this structure in mice. Indeed, when cutting through this structure, the many
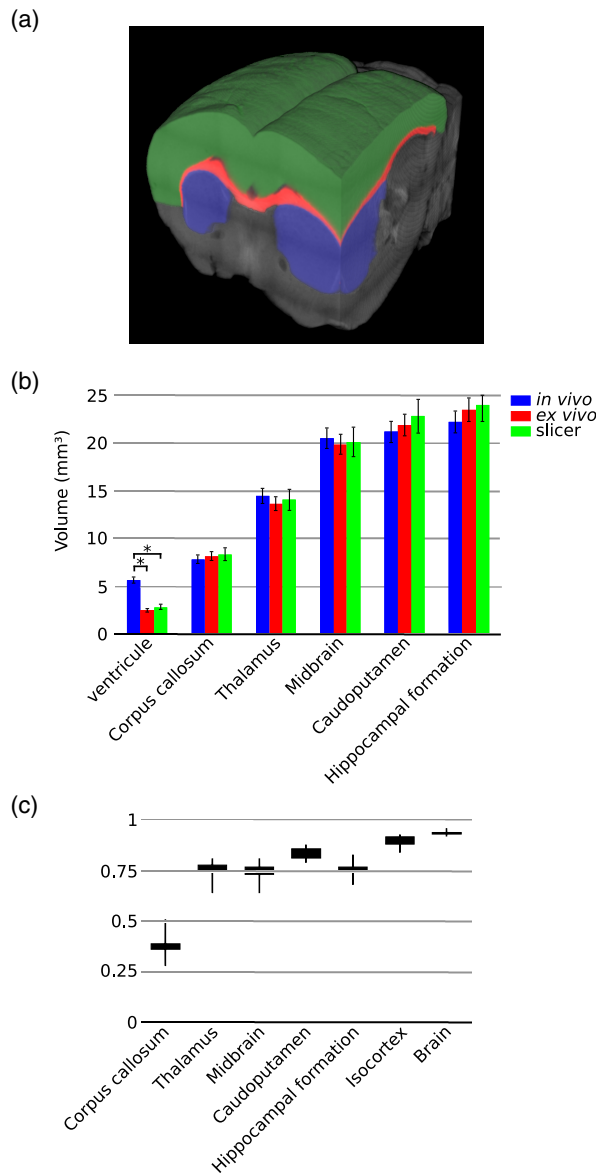
where A corresponds to the volume occupied by a brain region for *ex vivo* MRI and B the volume occupied of the corresponding brain region for slicer imaging. The Jaccard coefficient when overlapping MRI *ex vivo* to slicer data was smallest for the corpus callosum (0.39) and remained steady for other deep brain structures: thalamus (0.71), midbrain (0.67), caudoputamen (0.83), and hippocampus (0.73) [Fig. 5(c)]. The isocortex gave the highest Jaccard index among large brain regions, rising at 0.90. As for the whole brain volume, an average overlap of 0.94 was observed among all eight brains.

Further investigation of the alterations induced by serial imaging was performed by computing cortical thickness. Using the labeled cortex of the mice provided in the Allen brain framework, we were able to obtain voxel-based thickness maps for the MRI and slicer imaging modalities. Thickness maps for all eight animals and three imaging modalities were spatially normalized to the slicer template for statistical comparison. Figure 6(a) gives the average thickness map for all eight mice imaged with the slicer platform superimposed on the slicer template brain. Distinct separations of the cortex and corpus callosum are visible at the inner part of cortical map showing

(a)

(b)

(c)

Fig. 5 Brain labeling. (a) Slicer reconstructed brain segmented by region. Green: isocortex, red: corpus callosum, and blue: caudoputamen. (b) Volume of large brain regions measured for all eight animals with three modalities. * denotes significant volume difference ($p < 0.05$). Error bars represent standard deviation. (c) Jaccard index showing overlap between labeled regions of MRI *ex vivo* and slicer imaged brains. Whiskers indicate the upper and lower quartiles.

folds may not be fully supported by the agarose matrix, which cannot fully penetrate in small sulci, thus leading to cutting artifacts. Also, imaging does not always begin at the exact same coronal section for individual brains. The registration algorithm will likely try to overcompensate for this absence of tissue. Indeed, the registration algorithm assumes that both images are complete and similar (i.e., they contain the same information). For example, a missing olfactory bulb in one image will be stretched to fit a complete brain, as the registration algorithm will assume that the former is only deformed and not missing. This effect can be reduced but not eliminated using registration masks. Finally, when slicing through the anterior part of the
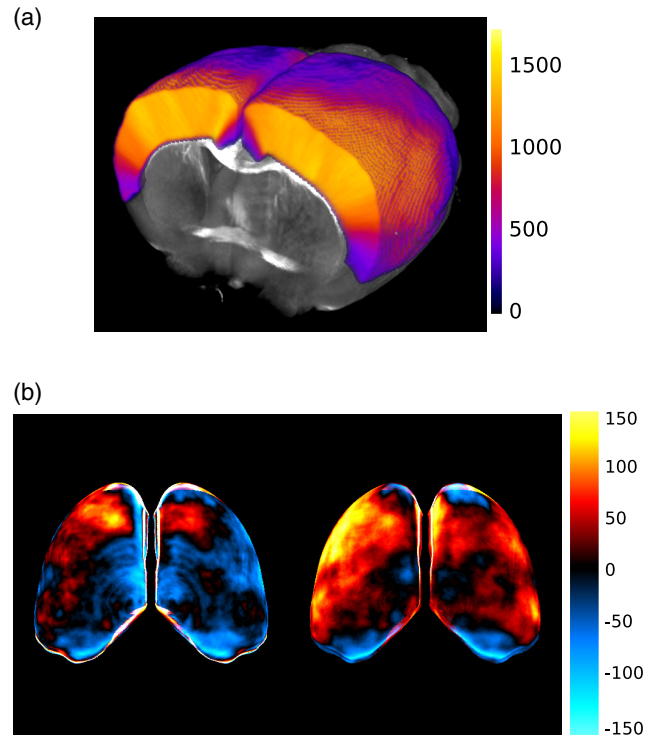
(a)

(b)

Fig. 6 Cortical thickness. (a) Average cortical thickness of mice imaged with slicer overlapped on slicer template brain. Scale bar in μm. (b) Top view of cortical surface, showing difference in cortical thickness between slicer and *in vivo* MRI imaging (left panel), *ex vivo* MRI imaging (right panel) and slicer imaging. Blue colors represent a thinning of the slicer brain cortex, while red colors represent a thickening. Scale bar in μm.

brain, it has happened that the last portion of the brain slipped out of the agarose mold due to smaller surface contact holding the brain in place. For certain brains, the most anterior part of the brain was missing, creating the shadow artifact present in the forebrain. Presumably, these issues can be alleviated with improvements in tissue preparation.

Warp field analysis showed that on average, a larger deformation of individual brains was needed to transpose to the template brain for OCT imaging compared to both *in vivo* and *ex vivo* MRI imaging. This could be due to deformation caused by vibratome sectioning of the tissue. Indeed, some areas are less supported by the agarose matrix such as the cerebellum, as described previously. Also, during the acquisition, brain tissue tends to detach itself from the agarose matrix, which can cause cutting artifacts. To address this problem,[15] we have oxidized agarose gels to enhance adherence with agarose. Another explanation for this large interindividual deformation could be that with slicer imaging, we do not image the exact same areas of the brain from one acquisition to another. As described above, acquisitions do not comprise the same parts of the cerebellum, sometime starting the acquisition at a more anterior part. The same goes for the olfactory bulb. As a result, some brains will be expanded to compensate for missing tissue while others will be shrunk. Nonetheless, the average OCT brain was very similar to the MRI *in vivo* template. Areas of largest displacement from one template to another, namely the olfactory bulb, the cerebellum, and optic nerve, are simply not present in the OCT template. Thus, the registration algorithm compensates for the absence by stretching these areas.

Large displacements, although to a lesser extent, also occur near the ventricular areas. This result corroborates with the large volumetric variations observed in ventricles when comparing *in vivo* to both *ex vivo* modalities. The intracranial pressure exercised on ventricles filled with cerebrospinal fluid maintains their shape. In the absence of intracranial pressure when performing *ex vivo* imaging, ventricles tend to collapse on themselves, explaining larger deformation. Despite these issues, anatomical measures showed no statistical differences among modalities suggesting that serial imaging could be used to assess anatomical markers.

OCT imaging in the fixed mouse brain gives rise to variable contrast in white matter, dependent on the fiber orientation, whereas gray matter contrast remains constant in all parts of the brain. When myelinated fibers run in the imaging plane of the objective, in this case parallel to coronal sections, they present a high reflectivity, represented as tissue with high intensity in the template. On the other hand, fibers oriented perpendicularly to the imaging plane will appear darker. This is particularly apparent in the caudoputamen where fibers oriented in different orientations appear with different intensity values. This particular interaction of white matter with light allowed to see the change in orientation of white fiber tracts in the posterior region of the corpus callosum and in the anterior commissure, as shown with diffuse tensor imaging.[42,43] Quantification of white matter tract orientation can be achieved using polarization sensitive OCT, allowing 3-D fiber tracking in the whole mouse brain at a higher resolution than could be achieved in diffuse tensor imaging.[3,44] Light sheet microscopy has also been used to image whole mouse brains.[45–47] This approach necessitates tissue clearing, which will disrupt native contrast of white and gray matter eliminating neuroanatomical features in the brain and rendering region labeling difficult. Tissue preparation needed for light sheet microscopy imposes harsh conditions to tissue and may further create deformations potentially altering the *in vivo* brain shape.

The labeling of OCT datasets was made possible by the combination of the ANTs toolbox and the Allen mouse brain. By registering individual OCT datasets to the Allen brain, we were able to automatically segment the brain in large regions. It was unclear at first though, whether we would be able to register datasets originating from different imaging modalities, showing different contrast information. The measure of the Jaccard index in large brain regions showed that our registrations were comparable to work previously done in MRI.[20,48] An exception remains for the corpus callosum, where a much lower overlap index was measured. The particular shape of the corpus callosum gives it a large surface to volume ratio, which has shown to influence greatly the Jaccard index.[49] The changing signal intensity of tissue within the corpus callosum can also explain poor registration.

The approach presented in this paper allows us to measure anatomical brain metrics, such as cortical thickness, in a single template space. The cortical thickness mapping relies on an adequately labeled cortex in the brain. The Jaccard index for the isocortex overlap was the highest among brain structures, confirming a robust labeling of the isocortex. The particular configuration of the isocortex, being at the surface of the brain, gives it well-defined borders that help for accurate registration to Allen brain.

5 Conclusion

In this paper, we presented an imaging platform capable of imaging entire mouse brains at microscopic resolution. The reasonable acquisition time allows imaging of large amounts of samples. We obtained for the first time a template brain of a population of mice using a microscopic OCT serial scanner and showed, through the comparison of brain region volume, cortical thickness, and overall brain volume, that fixation and slicing of the tissue generated little changes in brain morphology. We also demonstrate that we could register whole brain OCT datasets to MRI using image registration tools. Registration of detailed and highly resolved OCT maps to *in vivo* MRI is limited by the lack of resolution and low contrast of the latter. Accurate registration is achievable when acquiring *ex vivo* MRI, where a higher resolution and a better structural contrast are present. The combination of block-face microscopy with OCT imaging of the brain proves to be an adequate tool for reliable representation of *in vivo* brains while keeping neuroanatomical features. Such a tool opens the way for studies of observing microscopic alterations in the whole brain among a large group of subjects.

Disclosures

Acknowledgments

References

1. A. Kremer et al., "Developing 3D SEM in a broad biological context: 3D SEM," *J. Microsc.* **259**(2), 80–96 (2015).
2. Y. Fu et al., "Ex vivo and in vivo imaging of myelin fibers in mouse brain by coherent anti-Stokes Raman scattering microscopy," *Opt. Express* **16**(24), 19396 (2008).
3. H. Wang, C. Lenglet, and T. Akkin, "Structure tensor analysis of serial optical coherence scanner images for mapping fiber orientations and tractography in the brain," *J. Biomed. Opt.* **20**(3), 036003 (2015).
4. D. L. Price et al., "High-resolution large-scale mosaic imaging using multiphoton microscopy to characterize transgenic mouse models of human neurological disorders," *Neuroinformatics* **4**(1), 65–80 (2006).
5. S. Kitamura et al., "Longitudinal white matter changes in Alzheimer's disease: a tractography-based analysis study," *Brain Res.* **1515**, 12–18 (2013).
6. J. Miyata et al., "Interfrontal commissural abnormality in schizophrenia: tractography-assisted callosal parcellation," *Schizophr. Res.* **97**(1–3), 236–241 (2007).
7. K. Wang et al., "Altered functional connectivity in early Alzheimer's disease: a resting-state fMRI study," *Hum. Brain Mapp.* **28**(10), 967–978 (2007).
8. A. Schmitt et al., "Schizophrenia as a disorder of disconnectivity," *Eur. Arch. Psychiatry Clin. Neurosci.* **261**(S2), 150–154 (2011).
9. A. Nair et al., "Impaired thalamocortical connectivity in autism spectrum disorder: a study of functional and anatomical connectivity," *Brain* **136**(6), 1942–1955 (2013).
10. K. Amunts et al., "BigBrain: an ultrahigh-resolution 3D human brain model," *Science* **340**(6139), 1472–1475 (2013).
11. A. Li et al., "Micro-optical sectioning tomography to obtain a high-resolution atlas of the mouse brain," *Science* **330**(6009), 1404–1408 (2010).
12. H. Wang, J. Zhu, and T. Akkin, "Serial optical coherence scanner for large-scale brain imaging at microscopic resolution," *NeuroImage* **84**, 1007–1017 (2014).

13. H. Wang et al., "Reconstructing micrometer-scale fiber pathways in the brain: multi-contrast optical coherence tomography based tractography," *NeuroImage* **58**(4), 984–992 (2011).
14. S. W. Oh et al., "A mesoscale connectome of the mouse brain," *Nature* **508**(7495), 207–214 (2014).
15. T. Ragan et al., "Serial two-photon tomography for automated ex vivo mouse brain imaging," *Nat. Methods* **9**(3), 255–258 (2012).
16. H. F. Wehrl et al., "Assessment of murine brain tissue shrinkage caused by different histological fixatives using magnetic resonance and computed tomography imaging," *Histol. Histopathol.* **30**(5), 601–613 (2015).
17. V. Weisbecker, "Distortion in formalin-fixed brains: using geometric morphometrics to quantify the worst-case scenario in mice," *Brain Struct. Funct.* **217**(2), 677–685 (2012).
18. J. B. Arous, "Single myelin fiber imaging in living rodents without labeling by deep optical coherence microscopy," *J. Biomed. Opt.* **16**(11), 116012 (2011).
19. S. W. Jeon et al., "A feasibility study of optical coherence tomography for guiding deep brain probes," *J. Neurosci. Methods* **154**(1–2), 96–101 (2006).
20. B. B. Avants et al., "A reproducible evaluation of ANTs similarity metric performance in brain image registration," *NeuroImage* **54**(3), 2033–2044 (2011).
21. C. V. Bowen, J. S. Gati, and R. S. Menon, "Robust prescan calibration for multiple spin-echo sequences: application to FSE and b-SSFP," *Magn. Reson. Imaging* **24**(7), 857–867 (2006).
22. K. L. Miller et al., "Diffusion imaging of whole, post-mortem human brains on a clinical MRI scanner," *NeuroImage* **57**(1), 167–181 (2011).
23. H. Benveniste et al., "Magnetic resonance microscopy of the C57BL mouse brain," *NeuroImage* **11**(6), 601–611 (2000).
24. K. A. Vermeer et al., "Depth-resolved model-based reconstruction of attenuation coefficients in optical coherence tomography," *Biomed. Opt. Express* **5**(1), 322 (2014).
25. M. Hohmann et al., "Extension of depth-resolved reconstruction of attenuation coefficients in optical coherence tomography for slim samples," *Proc. SPIE* **9792**, 97920P (2015).
26. J. Lefebvre et al., "Whole mouse brain imaging using optical coherence tomography: reconstruction, normalization, segmentation, and comparison with diffusion MRI," *Neurophoton* **4**(4), 041501 (2017).
27. N. J. Tustison et al., "N4ITK: improved N3 bias correction," *IEEE Trans. Med. Imaging* **29**(6), 1310–1320 (2010).
28. S. van der Walt et al., "scikit-image: image processing in Python," *PeerJ* **2**, e453 (2014).
29. N. Otsu, "A threshold selection method from gray-level histograms," *IEEE Trans. Syst. Man Cybern.* **9**(1), 62–66 (1979).
30. P. Marquez-Neila, L. Baumela, and L. Alvarez, "A morphological approach to curvature-based evolution of curves and surfaces," *IEEE Trans. Pattern Anal. Mach. Intell.* **36**(1), 2–17 (2014).
31. L. Alvarez et al., "Morphological snakes," in *IEEE Conf. on Computer Vision and Pattern Recognition*, pp. 2197–2202 (2010).
32. B. B. Avants et al., "The Insight ToolKit image registration framework," *Front. Neuroinf.* **8**, 44 (2014).
33. B. Avants et al., "Symmetric diffeomorphic image registration with cross-correlation: evaluating automated labeling of elderly and neuro-degenerative brain," *Med. Image Anal.* **12**(1), 26–41 (2008).
34. L. Kuan et al., "Neuroinformatics of the Allen mouse brain connectivity atlas," *Methods* **73**, 4–17 (2015).
35. B. B. Avants et al., "The optimal template effect in hippocampus studies of diseased populations," *NeuroImage* **49**(3), 2457–2466 (2010).
36. K. L. Double et al., "Topography of brain atrophy during normal aging and Alzheimer's disease," *Neurobiol. Aging* **17**(4), 513–521 (1996).
37. J. S. Kwon et al., "Left planum temporale volume reduction in schizophrenia," *Arch. Gen. Psychiatry* **56**(2), 142 (1999).
38. S. E. Jones, B. R. Buchbinder, and I. Aharon, "Three-dimensional mapping of cortical thickness using Laplace's equation," *Hum. Brain Mapp.* **11**(1), 12–32 (2000).
39. C. Leahy, H. Radhakrishnan, and V. J. Srinivasan, "Volumetric imaging and quantification of cytoarchitecture and myeloarchitecture with intrinsic scattering contrast," *Biomed. Opt. Express* **4**(10), 1978 (2013).
40. J. Lefebvre, A. Castonguay, and F. Lesage, *OCT Mouse Brain Templates*, Mendeley Data, v1 (2017).
41. R. Quester and R. Schröder, "The shrinkage of the human brain stem during formalin fixation and embedding in paraffin," *J. Neurosci. Methods* **75**(1), 81–89 (1997).
42. Y. Jiang and G. A. Johnson, "Microscopic diffusion tensor imaging of the mouse brain," *NeuroImage* **50**(2), 465–471 (2010).
43. D. Wu et al., "In vivo high-resolution diffusion tensor imaging of the mouse brain," *NeuroImage* **83**, 18–26 (2013).
44. Y. Wang et al., "Histology validation of mapping depth-resolved cardiac fiber orientation in fresh mouse heart using optical polarization tractography," *Biomed. Opt. Express* **5**(8), 2843 (2014).
45. H.-U. Dodt et al., "Ultramicroscopy: three-dimensional visualization of neuronal networks in the whole mouse brain," *Nat. Methods* **4**(4), 331–336 (2007).
46. M. K. Schwarz et al., "Fluorescent-protein stabilization and high-resolution imaging of cleared, intact mouse brains," *PLoS One* **10**(5), e0124650 (2015).
47. R. Tomer et al., "Advanced CLARITY for rapid and high-resolution imaging of intact tissues," *Nat. Protoc.* **9**(7), 1682–1697 (2014).
48. A. Klein et al., "Evaluation of 14 nonlinear deformation algorithms applied to human brain MRI registration," *NeuroImage* **46**(3), 786–802 (2009).
49. T. Rohlfing et al., "Evaluation of atlas selection strategies for atlas-based image segmentation with application to confocal microscopy images of bee brains," *NeuroImage* **21**(4), 1428–1442 (2004).

Biographies for the authors are not available.